

Unconventional magnetization textures and domain-wall pinning in Sm–Co magnets

L. Pierobon¹, A. Kovács², R. E. Schäublin¹, U. Wyss³, R. E. Dunin-Borkowski², J. F. Löffler¹, M. Charilaou^{1,4}

¹*Laboratory of Metal Physics and Technology, Department of Materials, ETH Zurich, 8093 Zurich, Switzerland*

²*Ernst-Ruska Centre for Microscopy and Spectroscopy with Electrons,*

Peter Grünberg Institute, Forschungszentrum Jülich, 52425 Jülich, Germany

³*Arnold Magnetic Technologies, Birr-Lupfig 5242, Switzerland and*

⁴*Present address: Department of Physics, University of Louisiana at Lafayette, Lafayette, LA 70504, USA*

The strongest magnets for high-temperature applications are Sm–Co based alloys characterized by a cellular microstructure with $\text{Sm}_2\text{Co}_{17}$ cells and SmCo_5 precipitates, intersected by elongated Zr-rich platelets. This elaborate geometry endows the material with remarkable magnetic hardness because it constitutes a dense domain-wall-pinning network. A precise understanding of the pinning mechanisms could enable the formation of stronger Sm–Co magnets, but experiment and theory have not yet converged to a unified model. Here, we show by comparing high-resolution Lorentz microscopy and micromagnetic simulations that the magnetization processes in Sm–Co magnets are an interplay between curling instabilities and pinning effects. Specifically, domain walls are nucleated at the intersections between Zr-rich platelets and $\text{Sm}_2\text{Co}_{17}$ cells, and become pinned at the SmCo_5 precipitates, through which they can tunnel only via the Zr-rich platelets. Further, we have observed exotic domain-wall structures, such as topologically non-trivial 2π and 3π domain walls involved in domain-wall annihilation. Based on our findings, we propose how the microstructure of Sm–Co magnets could be optimized to increase the coercivity and remanence of the Sm–Co magnets.

I. INTRODUCTION

Sm–Co-based materials are among the strongest magnets available today, particularly for vital high-temperature precision applications thank to their high Curie temperature [1–3]. Extensive research and industrial development in the past few decades has lead to a significant improvement in the magnetic performance of Sm–Co magnets [4]. One such example is a highly engineered Sm–Co based system that consists of a cellular microstructure with $\text{Sm}_2\text{Co}_{17}$ cells enclosed by SmCo_5 precipitates (cell boundaries) and intersected by the so-called Z phase (Zr-rich platelets) perpendicular to the c -axis of the structure, which is at the same time the magnetic easy axis [1, 5, 6]. This characteristic geometry results from tailored aging heat treatments [1], and corresponds to a network of intertwined magnetically soft ($\text{Sm}_2\text{Co}_{17}$) and hard (SmCo_5) regions.

Combinations of hard and soft structures are highly tunable because they make use of the high saturation magnetization of the soft phase and the strong magnetocrystalline anisotropy of the hard phase [7, 8]. Particular attention has been devoted to modeling the Sm–Co cellular microstructure [9–12] in order to predict the coercivity. The enhanced coercivity in these cellular Sm–Co magnets emerges due to the difference between the magnetocrystalline anisotropies of the two phases and consequently the difference of domain-wall energy [9]. While conventional wisdom states that this microstructure constitutes a pinning system for domain walls, the exact magnetization processes remain elusive despite the intense research activities to understand the interaction of domain walls with the SmCo_5 precipitates [13–19].

Imaging experiments, by means of Lorentz transmission electron microscopy (LTEM), magnetic force microscopy, and Kerr microscopy, have revealed that do-

main walls follow the SmCo_5 precipitate morphology [17, 19–24], thus confirming strong pinning at the cell boundaries. Theory and experiment, however, have yet to converge on the role of the Z phase in the magnetic properties of this material [9–12]. Forward modeling of the Z phase is impeded by the fact that the material parameters of this phase cannot be easily estimated as the thickness of the Zr-rich platelets varies from material to material, which can be as thin as 1-2 atomic layers, and thus cannot be compared with measurements on bulk samples [25]. Hence, high-resolution imaging of the magnetization textures is crucial to elucidate the interplay between the soft, hard, and Z phases, and unveil the magnetization processes at play in the cellular Sm–Co magnets.

Here we present a detailed study of the magnetic state in a cellular Sm–Co magnet containing Fe, Cu and Zr, where we show high-resolution LTEM imaging of the domain-wall structure and systematically compare it to detailed micromagnetic simulations. By matching experiments and theory one-to-one we show that the magnetization processes in cellular Sm–Co magnets stem from an interplay between pinning at the $\text{Sm}_2\text{Co}_{17}$ cell boundaries and curling instabilities at the intersections between the Z-phase and the $\text{Sm}_2\text{Co}_{17}$ cells.

II. RESULTS

Our study is based on a $\text{Sm}(\text{Co},\text{Fe},\text{Cu},\text{Zr})_{7.57}$ industrial sample from Arnold Magnetic Technologies (see Methods section) and we begin our discussion by examining its microstructure. Figure 1 **a** shows an overview of the microstructure revealing the typical soft cells enclosed by the hard shells and intersected by the Z-phase platelets. A close-up view in Fig 1b and the corresponding chem-

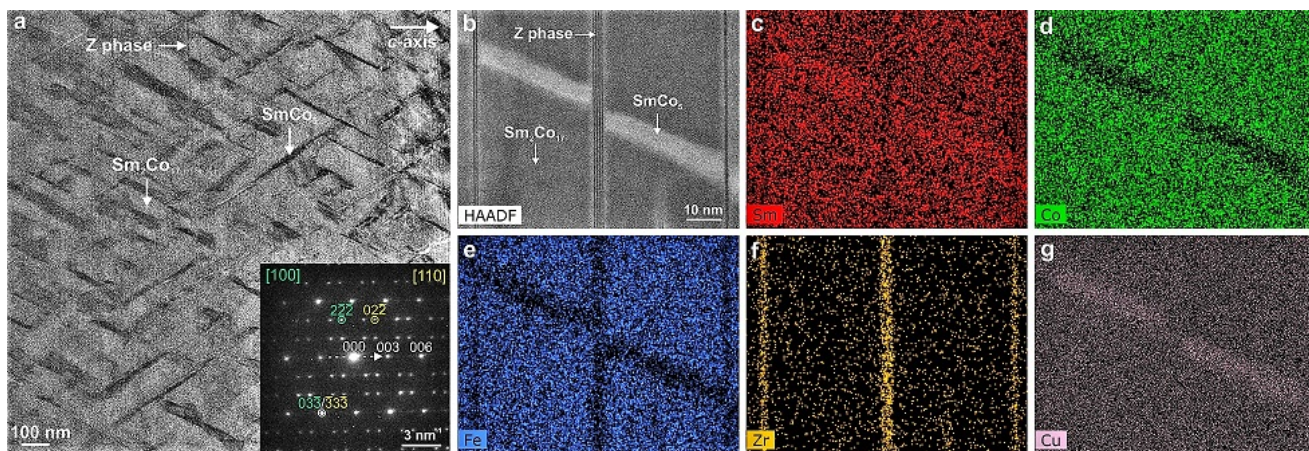


FIG. 1. **Sm-Co microstructure.** **a** Bright-field TEM image of a Sm-Co magnet showing cells of $\text{Sm}_2\text{Co}_{17}$ (light grey) enclosed by a network of SmCo_5 (dark grey) precipitates and the entire structure intersected by Zr-rich platelets (Z phase). The corresponding diffraction pattern, shown in the bottom right corner, contains reflections from the [100] (green) and [110] (yellow) directions (see Suppl. Fig. 1) **b** High-angle annular dark-field scanning TEM image showing the details of the microstructure accompanied by energy-dispersive spectroscopy (EDS) chemical maps of **c** Sm, **d** Co, **e** Fe, **f** Zr and **g** Cu, illustrating the distribution of the elements in the matrix and precipitates.

ical maps in Fig2c–g show sharp interfaces between the three phases. The thickness of the interface between $\text{Sm}_2\text{Co}_{17}$ and SmCo_5 ranges from atomically sharp to 2 nm, whereas the interfaces with the Z phase are always atomically sharp. The c -axis of the crystal structure (see Fig. 1 in the Supplementary Material) lies inside the TEM lamella, and the Z platelets are always perpendicular to the c -axis [6].

Note that the sharpness of the cell boundary and the even distribution of Cu in SmCo_5 do not suggest a Cu-rich interface between the 2:17 and 1:5 phase, which might critically affect the magnetic properties [24]. The $\text{Sm}_2\text{Co}_{17}$ cells are typically around 200 nm wide across their widest region, the SmCo_5 precipitates are around 10 nm thick, and the Z platelets are at most 5 nm thick and thus consist of only a few atomic layers (some platelets are made out of only 1 to 2 atomic layers). As we will discuss below, it is the thickness of the Z platelets that plays a crucial role in the magnetic properties.

Figure 2 shows Lorentz TEM images of the cellular Sm–Co magnet in a thermally demagnetized state. Fig. 2a and b show over- and under-focus images, respectively, in order to confirm the imaging of domain walls, which appear as alternating sharp and bright contrast (convergent), or blurry and dark contrast (divergent), depending on the sense of the magnetization profile along the domain wall. These images reveal an astonishing domain-wall pattern that follows exactly the microstructure of the material, similar to those shown in the literature [17, 19–21]. Specifically, we observe that the domain walls are always adjacent to the SmCo_5 precipitates and are offset by around 50 nm via the Z phase exactly where they intersect the precipitates. Even though LTEM does not enable a quantification of the direction of the magnetization along the domain-wall profile, considering the high uniaxial anisotropy in the system we may assume that these are π Bloch-type domain walls [17], as our simulations will also confirm below. The average domain-wall thickness was estimated from a series of images taken at different defocus values (see Fig. 2 in the Supplementary Material) to be 4 ± 2 nm, which is in agreement with theory, considering the properties of $\text{Sm}_2\text{Co}_{17}$ from which $\delta_{\text{dw}} = \sqrt{A/K_{\text{u}}} = 2.7$ nm, where A is the exchange stiffness and K_{u} is the uniaxial magnetocrystalline anisotropy (see Methods). This result suggests that the domain walls are mostly located in the soft $\text{Sm}_2\text{Co}_{17}$ phase, reminiscent of an exchange spring magnet.

While the zig-zag domain-wall structure is quite well known, here we observe for the first time unexpected domain-wall patterns at some of the intersections between the three phases, where domain walls with opposite sense meet and cancel each other out (marked with an arrow in 2a and b). Surprisingly, domain walls with higher winding can be observed, i.e. 2π and even 3π walls, as shown in Fig. 2c. The unwinding of such domain walls is non-trivial and requires a violation of topological constraints, which start with curling instabilities at the in-

tersection between the soft and the Z phase. Therefore, these exotic magnetization textures are closely associated with the microstructure and indicate that topological aspects need to be considered in order to correctly interpret the magnetic state.

Given the elaborate microstructure, these observations raise additional questions regarding the magnetic state in cellular Sm–Co magnets. In order to obtain further insight, we performed detailed high-resolution micromagnetic simulations to investigate the formation of the observed complex domain-wall patterns. To this end, it is imperative that we fully consider the microstructure in a realistic way. Hence, we constructed simulation systems directly from the TEM images shown above. Figures 3a,b show how we have truncated the microstructure to obtain a system with the three phases in the exact same geometry and scale.

In our simulations, we considered the ferromagnetic exchange and uniaxial anisotropy energies, dipole-dipole interactions, and the exchange energy between the three different phases. The material parameters (A , K_{u} , and saturation magnetization M_{s}) are well known and were taken from the literature [6, 24–26] (see Methods). The exchange interaction energy between the three phases, however, is unknown. We have performed parametric micromagnetic studies where we varied the exchange interaction and compared the theoretical hysteresis curve with the experimental data, thus deducing the correct values by matching simulations and experiments (Fig. 3c-e).

As mentioned above, the precise material properties of the Z phase are unknown because the exact chemical composition is unclear and the size of the platelets can be as small as a single atomic layer (see Fig. 1b). All material parameters, e.g., exchange stiffness, saturation magnetization, and magnetocrystalline anisotropy are affected by the reduced dimensions of the platelets and their interfaces [27]. It is known from thin film studies that the anisotropy is the most sensitive property and changes drastically depending on the thickness and local atomic arrangements [28]. We have therefore performed simulations where we considered the Z phase to be either anisotropic or isotropic. In the former case, we assigned the bulk value of K_{u} [6, 25], whereas in the latter case we set $K_{\text{u}} = 0$. From the comparison of experimental and theoretical $M(H)$ curves, we find that the simulations match the experimental observations only if $K_{\text{u}} = 0$. Hence, for the rest of the discussion we assume that the Z phase only has shape anisotropy.

In order to make our simulation quantitatively comparable the experimental results, we matched theoretically predicted coercivity with the experimental one by varying the exchange energy between the three different phases. We find that the coercivity increases with decreasing exchange energy between the three phases (see Fig. 3c). This supports experiments showing that increasing Cu content leads to higher coercivities, depending on the compositional gradient at the boundary [22, 24], due to

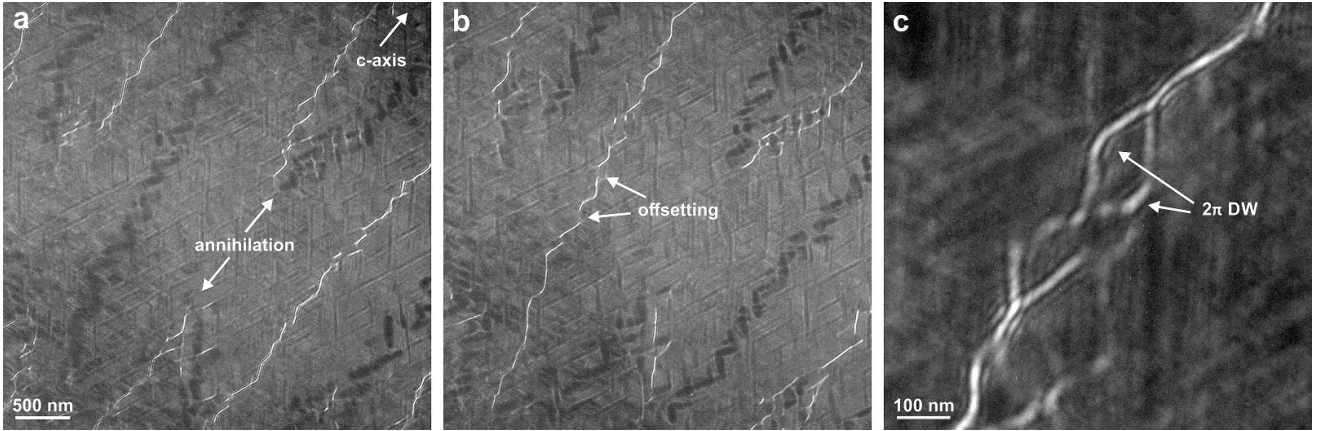


FIG. 2. **Magnetic domain structures in the cellular Sm–Co magnet.** Overview of domain walls imaged by LTEM in 0.5 mm **a** over- and **b** underfocus. Domain walls appear sharp bright (convergent) or dark (divergent) depending on the sense of the magnetization along the wall profile and defocus. Inverting the defocus inverts the contrast, thus confirming the domain-wall structures, which are in this case characterized by domain-wall annihilation and offsetting. **c** Close-up showing an intricate domain-wall structure with branching and alternate π and 2π magnetization profiles.

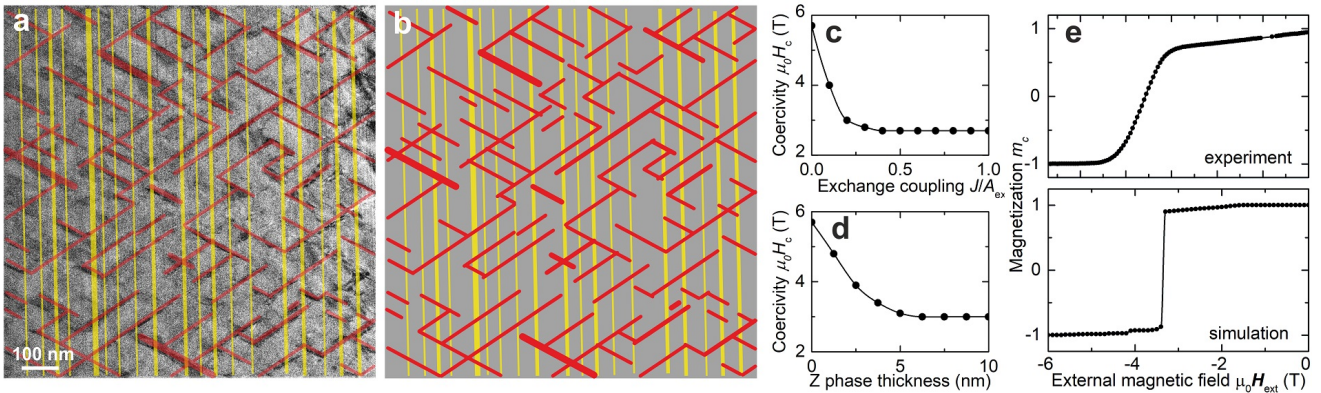


FIG. 3. **Modelling the microstructure of the cellular Sm–Co magnets.** **a** Truncation of the microstructural features of Sm–Co, as seen in Fig. 1a, to create a model shown in **b** with the $\text{Sm}_2\text{Co}_{17}$ matrix (grey), the SmCo_5 precipitates (red), and the Z-phase (yellow). **c** Dependence of the coercivity as a function of exchange coupling between the individual phases, illustrating that smaller exchange between the phases leads to higher coercivity. Using these results, we can compare the theoretical coercivity with that of real samples. **d** Dependence of the coercivity on the thickness of the Z phase, showing that it decreases exponentially with decreasing thickness. **e** Comparison between an experimentally measured $M(H)$ loop at $T = 300$ K and a simulated loop. By matching the simulation to the 300 K experimental data, we are adapting the exchange stiffness in the system to correspond to the configuration at that temperature. The external field is applied parallel to the c axis, i.e., perpendicular to the Z-phase platelets.

the formation of Cu-rich interfaces between the magnetic phases that decrease the exchange coupling.

We have also found that changing the thickness of the SmCo_5 precipitates does not modify the magnetic performance strongly, in agreement with experiments [29] and theory [30], showing that the pinning field is saturated for a SmCo_5 thickness of more than 4 nm. This contradicts the predictions by Fidler et al. [10, 12], stating that the SmCo_5 thickness should be at least three times the exchange length ($3\delta_{\text{exc}} \approx 20$ nm) for effective domain-wall pinning. The pinning, however, is a complex process and depends strongly on the Cu content in the SmCo_5 precipitates [31]. In our experiments we have not found any observable Cu-composition gradient, and hence we considered a homogeneous Cu-rich SmCo_5 precipitate.

Furthermore, we have found that the coercivity strongly depends on the Z phase thickness (see Fig. 3d). In the absence of the Z phase, it has a maximum value of 5.7 T, and decreases exponentially with increasing Z phase thickness until the thickness of 5 nm, where it reaches a minimum of 3 T and remains constant at higher thicknesses. These results explain recent experimental observations, where the magnetic performance deteriorated with increasing Z phase thickness [19]. However, since Zr is essential in forming this microstructure [20], it cannot be completely eliminated from the material, but the Z phase platelets should be as thin as possible to maximize the performance. As we will discuss below, smaller thickness impedes magnetization curling and hence a stronger external field is required to initiate the magnetization reversal process, which begins at the intersections of the Z and $\text{Sm}_2\text{Co}_{17}$ phases.

In the simulations that we discuss in the following, the thicknesses of the cell boundary and the Z phase were derived directly from the TEM images, where we have 10 nm thick SmCo_5 precipitates and 1 to 5 nm thick Z phase precipitates. Figure 3e shows an experimentally measured and a simulated $M(H)$ curve, confirming the agreement between experiment and theory regarding the coercivity and the general form of the curve, with a gradual decrease of the magnetization upon reversing the external field prior to the full magnetization switching at 3.4 T. Our simulations indicate that the gradual decrease is due to the isotropic defects that reverse their magnetization earlier than the rest of the material, which is yet another confirmation that defects do not exhibit significant magnetocrystalline anisotropy. Note that the $M(H)$ curves are not identical, because the experimental one is measured on a bulk sample, where we have gradual switching of parts of the material, while the theoretical one is simulated for a thin lamella. Further, the lamella with a thickness/width aspect ratio of about 1/1000 has an additional shape anisotropy, though much smaller than the magnetocrystalline anisotropy $K_u \gg \mu_0 M_s^2/2$.

In order to study the domain-wall patterns in cellular Sm-Co magnets, we start our simulation with three straight domain walls and minimize the energy. Figure 4 shows the results as contour plots of the magnetiza-

tion, overlaid onto the microstructure. Note the striking resemblance of Fig. 4a with the LTEM images of Fig. 2: the domain walls follow exactly the SmCo_5 shell geometry, including the offset by the Z phase platelets. Fig. 4b shows a close-up image of the magnetization texture around intersections between the three phases for the region marked with a square in Fig. 4a. From these images we deduce a domain-wall thickness in the SmCo_5 and the $\text{Sm}_2\text{Co}_{17}$ phases of 1.5 nm and 4.7 nm, respectively, which are slightly larger than the theoretically expected values of 1.2 nm and 2.7 nm using the equation $\delta_{\text{dw}} = \sqrt{A/K_u}$. This suggests that the presence of the Z phase, which does not have magnetocrystalline anisotropy, significantly affects the shape of the domain walls, and also agrees with our experimental observation of the domain-wall thickness of 4 ± 2 nm (see Suppl. Fig. 1), confirming our conclusion that the domain walls are mostly located in $\text{Sm}_2\text{Co}_{17}$. Notably, the domain walls inside the Z phase are extremely thin, and the moments turn away from the c -axis due to the dominating shape anisotropy of the platelets. This indicates that the domain walls between the Sm-Co phases and the Z phase are in fact $\pi/2$ domain walls. To minimize the exchange energy associated with it, the magnetic moments are twisted with opposite handedness at the edges of the SmCo_5 cell boundary. This is further analyzed in Fig. 4c, which shows a detailed view of a region where the three phases intersect and a domain wall propagates through all of them. We observe a narrow domain wall in the SmCo_5 precipitate, a broader wall in the $\text{Sm}_2\text{Co}_{17}$ cell, and a tilting of the moments away from the c -axis inside the Z phase. The domain wall is in fact injected into the hard phase at the location where the three phases meet. These results shed new light on previous observations based on electron microscopy [23], which suggested a tilting of the magnetic flux away from the easy axis around intersections. This validates our modelling strategy, especially the assumption that the Z phase does not exhibit substantial magnetocrystalline anisotropy, but that it is dominated by shape anisotropy.

The points in the microstructure where the three phases intersect play a critical role in the magnetization process because their edges with different material properties enable curling instabilities. We show in Fig. 4e-h the process of magnetization reversal, i.e., coming from a saturated state and applying the external field in the opposite direction. The demagnetization starts at the intersections between the Z phase and the soft phase in the form of nucleating domain walls which gradually grow inside the $\text{Sm}_2\text{Co}_{17}$ cells, and become pinned by the hard cell boundaries. The domain-wall growth then progresses through the intersections where all three phases meet and crosses to the adjacent soft phase cell through these points. This further indicates that the Z phase does indeed play a vital role in the magnetization process, which is an interplay between curling instabilities at intersections between the Z phase and soft cells, and pinning at the hard precipitates.

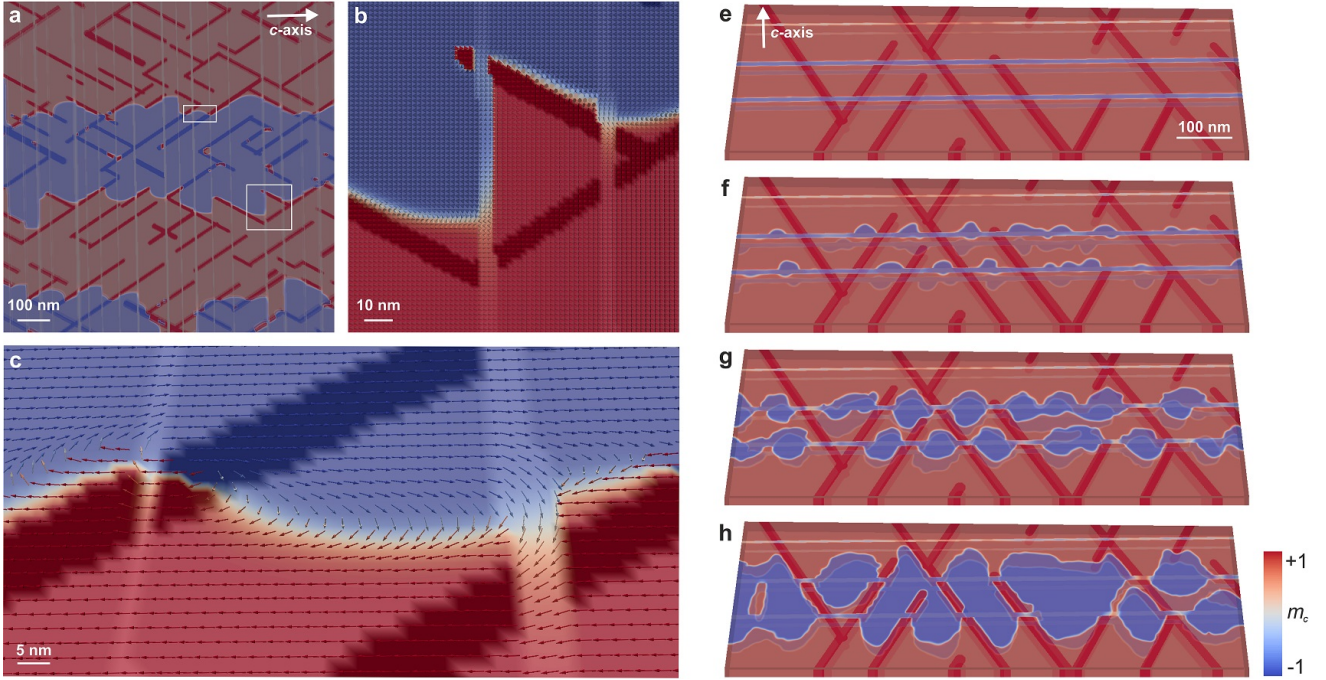


FIG. 4. **Simulation of 3D domain-wall structures and nucleation in the cellular Sm-Co magnet.** **a** Structure with four domains in a demagnetized state showing that domain walls are pinned to the microstructural features, specifically the SmCo_5 precipitates, and are offset by the Z phase. **b** Close-up of the marked square area in **a** reveals that the domain walls begin at the phase boundary between $\text{Sm}_2\text{Co}_{17}$ and SmCo_5 and are mostly situated inside $\text{Sm}_2\text{Co}_{17}$. **c** Detailed view of the magnetization texture at the intersection of all three phases, showing how a domain wall can be injected into the hard phase through a Z phase platelet, and consequently how its thickness varies between the two phases. **e-h** Illustration of the magnetization reversal process at a slightly supercritical field, i.e., larger than the switching field, parallel to the c -axis: as time progresses domains with magnetization parallel to the field begin nucleating at the Z phase and spread inside the $\text{Sm}_2\text{Co}_{17}$ phase, but their growth is impeded by the SmCo_5 precipitates (the time step between each figure is 0.1 ns). The color scale bar for the magnetization is the same for all panels.

Importantly, this demagnetization process is also responsible for the formation of domain walls with higher winding, such as those observed by LTEM in Fig. 2. We have investigated this further by comparing the simulated domain-wall structures with those observed in the experiment. The left-hand panels in Fig. 5 show LTEM images of the thermally demagnetized state (5a) and the remanent state (5c), and the right-hand panels show the corresponding simulated magnetization textures overlaid onto the TEM images of the exact same microstructure. The LTEM image in Fig. 5a was captured with 0.25 mm overfocus and the image in 5c was captured with 0.8 mm overfocus. The reason for the increased defocus was to enhance the magnetic contrast in order to reveal the finer domain-wall structure in the remanent state.

Fig 5a reveals the domain-wall structures zigzagging through the microstructure following the precipitate geometry and being offset by the Z phase, identical to the patterns shown in Fig. 2. In Fig. 5c we observe that even though the sample is nearly saturated (as we know from Fig. 3e, the remanent state corresponds to $M = 0.95M_s$), the material contains a large number of domain walls that separate domains with parallel magnetization, that is, domain-walls with 2π or higher winding. Fig. 5b and d show the simulated magnetization state, which shows features that are in precise analogy to the experimentally observed patterns: in all cases the domain walls follow the precipitate geometry, and in the remanent state we find distinct 2π domain walls, essentially enclosing isolated SmCo_5 precipitates (indicated by an arrow in Fig. 5d). The striking similarity between the experimentally observed domain walls and those predicted by simulations once more confirms our interpretation of the magnetic state in this system.

III. CONCLUSIONS

We have shown with LTEM images and micromagnetic simulations that there are sharp magnetic domain walls in cellular Sm-Co magnets that follow exactly the morphology of the hard-phase precipitates and are offset at intersections of the precipitates with the Z phase platelets. Based on our finding that the domain walls are mostly in the $\text{Sm}_2\text{Co}_{17}$ phase, reminiscent of an exchange spring system [32], we may propose that the thickness of SmCo_5 precipitates could be reduced to the minimum, considering that the domain walls in SmCo_5 are only about 1.5 nm wide. Importantly, we have confirmed that the Z phase plays a crucial role in the magnetization process as curling instabilities at the intersections between the soft and Z phase act as nucleation sites for domain walls upon reversing the external magnetic field. The domain walls propagate inside the soft cells and become pinned at the hard precipitates. They can only propagate through the intersections between the precipitates and the Z phase. Hence, we propose that both the Zr and Sm contents could be reduced in this system. This

would result in finer Zr platelets, which would impede magnetization switching, and the reduced Sm would lead to smaller SmCo_5 precipitates, which would in turn increase remanence, leading to a much more powerful magnet. Additionally, where all three phases meet, we have observed exotic domain-wall structures with 2π and possibly higher winding as well as domain-wall annihilation. These exotic, topologically non-trivial domain walls need to be studied further in order to understand the physics of multi-phase magnets in detail and allow us to fully harness the potential of these high-performance materials.

IV. METHODS

A. Sample synthesis

The alloying elements were melted in an induction furnace under vacuum and the alloy was cast in a metallic book mold. After crushing with a hammer mill, the powder was milled in a jet mill to a powder with a particle size of 4 – 8 μm . The powder was filled in a rubber mold, aligned with magnetic pulses with field strength of about 5 T and pressed in an isostatic press with 3000 MPa. The green parts were sintered under vacuum at a temperature of 1200–1220 $^\circ\text{C}$, solution annealed at 1170–1200 $^\circ\text{C}$ and quenched with an inert gas to room temperature. Subsequently, the parts were tempered at 850 $^\circ\text{C}$, slowly cooled to 400 $^\circ\text{C}$, and then quenched to room temperature.

The overall chemical composition of the final material was $\text{Sm}(\text{Co}_{0.695}, \text{Fe}_{0.213}, \text{Cu}_{0.07}, \text{Zr}_{0.022})_{7.57}$ with minor additional oxygen content in the form of Sm_2O_3 .

B. Magnetometry

The magnetization of a small piece of the sample was measured as a function of external field at room temperature using a Superconducting Quantum Interference Device (SQUID) in a Magnetic Property Measurement System (MPMS3) by Quantum Design.

C. Transmission Electron Microscopy

Electron transparent specimens for TEM studies were prepared using Ga ion sputtering in a dual beam focused ion beam (FIB) scanning electron microscope (SEM) workstation and a conventional lift-out method. The ion beam induced damage on the surfaces was reduced by low-energy (< 1 keV) Ar ion milling using a Fischione Nanomill system. The thickness of the lamellae was measured on a FEI Tecnai F30 FEG Transmission Electron Microscope (TEM) using Electron Energy Loss Spectroscopy (EELS), and we obtained a uniformly varying range of thicknesses between 80 - 140 nm.

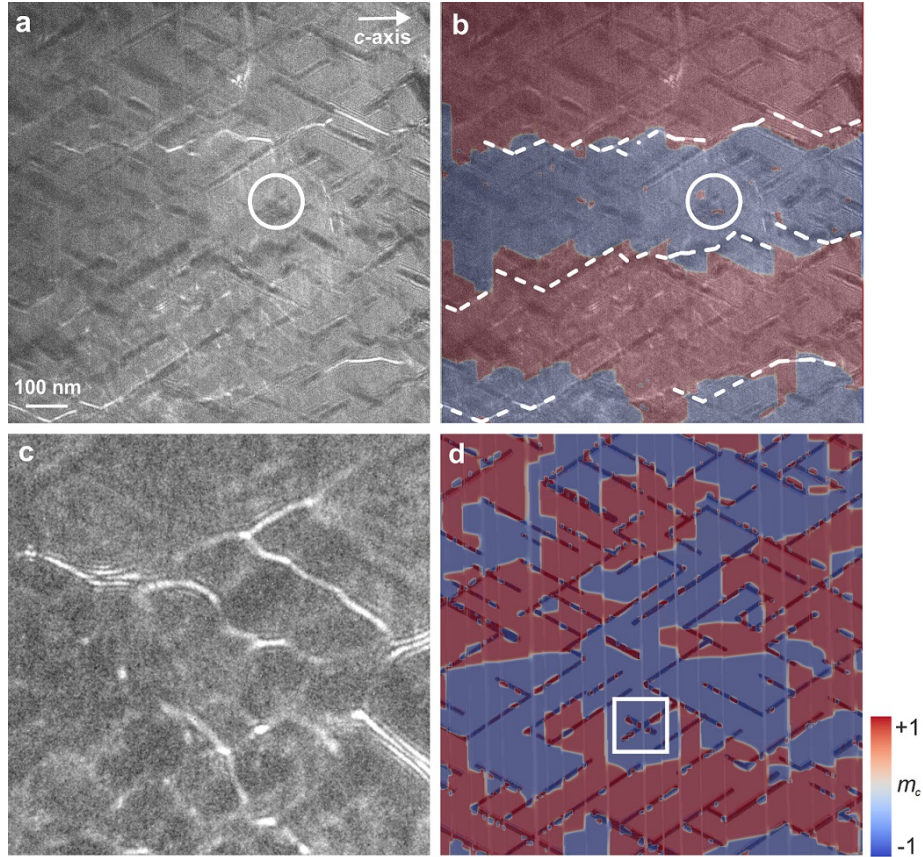


FIG. 5. **Comparison between experiment and theory.** **a** LTEM of the region from Fig. 1a **a** shows three domain walls at 0.24 mm overfocus and **b** the same image superimposed on a simulated scenario of three domain walls in the same microstructure. Note the striking resemblance of the domain-wall network, which is pinned at SmCo_5 and offset by the Z phase. Surprising 2π domain walls are shown in the white circle. **c** LTEM of $\text{Sm} - \text{Co}$ after applying an external field of 6 T at 0.8 mm underfocus. The domains are smaller and the domain-wall structure is highly elaborate, representing the initial nucleation stages of the magnetization process. **d** Simulated scenario of **c** once again confirming the astonishing agreement between experiment and theory with branching domain walls pinned at SmCo_5 . An example of high winding domain walls, i.e. 3π or more, is indicated in the white rectangle. Note that **c** and **d** do not show the same region, but only a qualitative comparison of the unconventional structures. All panels have the same scale bar.

The Sm–Co specimens were studied at remanence in magnetic-field-free (Lorentz mode) conditions using a spherical aberration corrected FEI Titan microscope operated at 300 keV. In Fresnel images, the intensity distribution at defocus Δz is recorded to reveal a bright (convergent) or dark (divergent) contrast at the positions of the magnetic domain walls. The net deflection of electrons from magnetic domains is induced by the Lorentz force, $\mathbf{F} = -ev \times \mathbf{B}$, where e is the electron charge, v is the velocity of the incident electrons and \mathbf{B} is the in-plane magnetic induction in the sample.

A conventional microscope objective lens was used to apply magnetic fields on the specimen. TEM images were recorded using a direct electron counting Gatan K2-IS camera and Gatan Microscopy Suite software.

D. Micromagnetic simulations

We have performed high-resolution micromagnetic simulations to investigate the link between the microstructure and the domain-wall network in Sm–Co magnets. The total energy density of the system consists of: (i) ferromagnetic exchange; (ii) uniaxial magnetocrystalline anisotropy; (iii) Zeeman coupling to an external magnetic field; and (iv) dipole-dipole interactions:

$$F = \sum_i [A^i (\nabla \cdot \mathbf{m}^i)^2 - K_u^i (m_c^i)^2 + \mu_0 M_S^i \mathbf{m}^i \cdot \mathbf{H}_{\text{ext}} - \frac{\mu_0 M_S^i}{2} \mathbf{m}^i \cdot \mathbf{H}_{\text{dip}} - \mu_0 M_S^i \mathbf{m}^i \cdot \mathbf{H}_{\text{exc}}], \quad (1)$$

where $\mathbf{m}^i = \mathbf{M}^i / M_S^i$ is the magnetization unit vector for phase i with M_S^i the saturation magnetization, A^i is the exchange stiffness, K_u^i is the first-order uniaxial anisotropy constant, \mathbf{H}_{ext} is the external magnetic field, \mathbf{H}_{dip} is the local demagnetizing field due to dipole-dipole interactions, and H_{exc} is the exchange field at the interfaces between different phases. The c -component of the magnetization is inside the lamella plane.

The material parameters were taken from the literature [6, 25, 26], and are $M_s = 1.05$ T, $A = 23.6$ pJ/m, and $K_u = 17.2$ MJ/m³ for SmCo₅, $M_s = 1.25$ T, $A = 24.7$ pJ/m, and $K_u = 3.3$ MJ/m³ for Sm₂Co₁₇, and $M_s = 0.37$ T, $A = 11$ pJ/m, and $K_u = 2.1$ MJ/m³ for the Z phase. Note that Cu in the SmCo₅ changes the material parameters by lowering A , M_s and K_u , but the composition of Cu in our material is less than 10% of the 3d metal content and the material parameters are not strongly reduced [24]. We performed tests with the material parameters of Sm(Co_{0.9}Cu_{0.1})₅ and found no qualitative difference in the behavior of the system.

The exchange field at the interface between two phases is proportional to $\frac{A^i}{M_s^i} \frac{A^j}{M_s^j} / \left(\frac{A^i}{M_s^i} + \frac{A^j}{M_s^j} \right)$. Based on our optimization, described in the main text, we found the following exchange values: (i) hard to soft 16 pJ/m; (ii) soft to hard 13 pJ/m; (iii) soft to Z phase 4.4 pJ/m; (iv)

Z-phase to soft 1.3 pJ/m; (v) hard to Z phase 2.7pJ/m; and (vi) Z phase to hard 0.95 pJ/m.

We have performed both energy minimization simulations and also solved the Landau-Lifshitz-Gilbert (LLG) equation of motion

$$\partial_t \mathbf{m} = -\gamma (\mathbf{m} \times \mathbf{H}_{\text{eff}}) + \alpha (\mathbf{m} \times \partial_t \mathbf{m}), \quad (2)$$

where γ is the electron gyromagnetic ratio, α is the dimensionless damping parameter, and $\mathbf{H}_{\text{eff}} = -\partial_{\mathbf{m}} F / \mu_0 M_S$ is the effective magnetic field in the material consisting of external and internal magnetic fields, which depend on the material parameters. The simulations have been done with mumax3[33], and the visualization of the magnetization textures was done with Paraview [34].

ACKNOWLEDGMENTS

LP, MC and JFL gratefully acknowledge funding from the Swiss National Science Foundation (Grant No. 200021-172934). We thank L. Grafalha Morales and A.-G. Bitterman for the preparation of the TEM samples, and gratefully acknowledge ScopeM ETH Zurich for the overall use of its facilities.

CORRESPONDENCE

Correspondence and requests for materials should be addressed to LP (email: leonardo.pierobon@mat.ethz.ch), JFL (email: joerg.loeffler@mat.ethz.ch) and MC (email: michalis.charilaou@louisiana.edu).

V. SUPPLEMENTARY INFORMATION

Supplementary Figure 1 shows a diffraction pattern of the sample shown in Fig 1 in the main text, which contains the reflections from [100] and [110] directions. The experimental and simulated patterns show an excellent agreement.

The width of the domain-wall contrast of 4 ± 2 nm at zero defocus was extrapolated from a series of LTEM images recorded at different defocus values, as shown in Sup. Fig. 2. It is worth mentioning that this approach usually gives a slight overestimate of the true domain-wall width. We also deduced the domain-wall width from the simulated systems by fitting the magnetization profile across the domain wall with $\tanh(r/\lambda)$, where r is the distance from the domain-wall center and $\lambda = \delta_{\text{dw}}/2$. The values for the domain-wall thickness in the simulated system for the SmCo₅ and the Sm₂Co₁₇ phases are 1.5 nm and 4.7 nm, respectively.

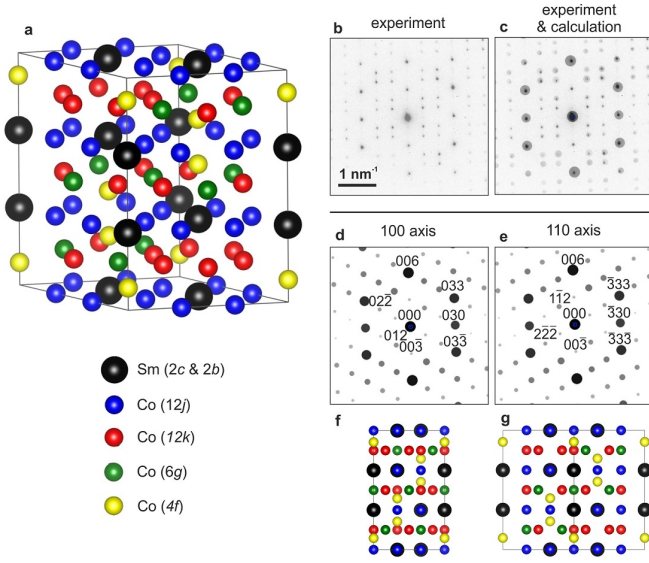


FIG. 6. **Crystal structure of Sm–Co:** **a** Unit cell of the $\text{Sm}_2\text{Co}_{17}$ phase showing the atomic sites for Sm (black) $2b$ and $2c$, and the 4 different atomic sites for Co: (blue) $12j$, (red) $12k$, (green) $6g$, and (yellow) $4f$. **b** shows the recorded diffraction pattern from one $\text{Sm}_2\text{Co}_{17}$ cell and **c** shows the calculated pattern overlaid on the experimental pattern, confirming the excellent agreement. The calculated pattern is a convolution of **d** [100] and **e** [110] reflections, and the corresponding crystal structure viewed along these directions is shown in **f** and **g**, respectively.

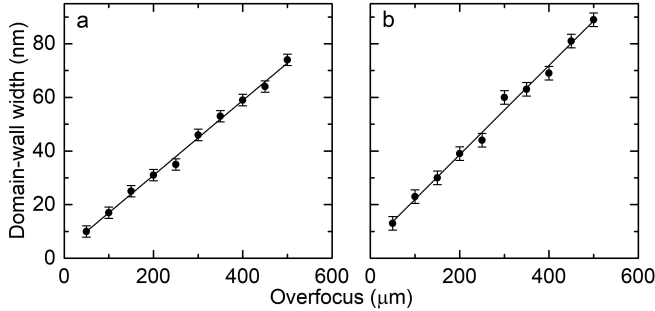


FIG. 7. **Measurements of domain-wall width.** **a-b** The thickness of two domain walls was obtained from a focal-series reconstruction. The apparent width of divergent domain walls (appearing as dark contrast) was measured for different values of defocus (data points). The real width of the domain walls was deduced from the intersection of the linear fit to the data points with the y-axis.

[1] Hadjipanayis, G. C. *et al.* High temperature 2:17 magnets: Relationship of magnetic properties to microstructure and processing. *IEEE Trans. Magn.* **36**, 3382 (2000).
 [2] Gutfleisch, O. *et al.* Magnetic materials and devices for the 21st century: Stronger, lighter, and more energy efficient. *Adv. Mat.* **23**, 821 (2011).
 [3] McCallum, R. W., Lewis, L. H., Skomski, R., Kramer,

M. J. & Anderson, I. E. Practical aspects of modern and future permanent magnets. *Annu. Rev. Mater. Res.* **44**, 451 (2014).
 [4] Horiuchi, Y. *et al.* Effects of solution treated temperature on the structural and magnetic properties of iron-rich $\text{Sm}(\text{CoFeCuZr})_z$ sintered magnet. *IEEE Transactions on Magnetism* **49**, 3221–3224 (2013).

- [5] Liu, J. F., Zhang, Y., Dimitrov, D. & Hadjipanayis, G. C. Microstructure and high temperature magnetic properties in $\text{Sm}(\text{Co,Cu,Fe,Zr})_z$ ($z = 6.7-9.1$) permanent magnets. *J. Appl. Phys.* **85**, 2800 (1999).
- [6] Duerrschnabel, M. *et al.* Atomic structure and domain wall pinning in samarium-cobalt-based permanent magnets. *Nat. Comm.* **8**, 54 (2017).
- [7] Kronmüller, H., Fischer, R., Seeger, M. & Zern, A. Micromagnetism and microstructure of hard magnetic materials. *J. Phys. D: Appl. Phys.* **29**, 2274 (1996).
- [8] Skomski, R. *et al.* Predicting the future of permanent-magnet materials. *IEEE Transactions on Magnetics* **49**, 3215–3220 (2013).
- [9] Skomski, R. Domain-wall curvature and coercivity in pinning type Sm–Co magnets. *J. Appl. Phys.* **81**, 5627 (1997).
- [10] Fidler, J. & Schrefl, T. Micromagnetic modelling – the current state of the art. *J. Phys. D: Appl. Phys.* **33**, R135 (2000).
- [11] Streibl, B., Fidler, J. & Schrefl, T. Domain wall pinning in high temperature $\text{Sm}(\text{Co,Fe,Cu,Zr})_{7-8}$ magnets. *J. Appl. Phys.* **87**, 4765 (2000).
- [12] Fidler, J. *et al.* Micromagnetic modelling and magnetization processes. *Journal of Magnetism and Magnetic Materials* **272-276**, 641–646 (2004).
- [13] Gaunt, P. Domain wall pinning as a source of magnetic hardening in alloys. *Journal of Applied Physics* **43**, 637–638 (1972).
- [14] Livingston, J. D. & Martin, D. L. Microstructure of aged $(\text{Co,Cu,Fe})_7\text{Sm}$ magnets. *J. Appl. Phys.* **48**, 1350 (1977).
- [15] Nagel, H. Coercivity and microstructure of $\text{Sm}(\text{Co}_{0.87}\text{Cu}_{0.13})_{7.8}$. *J. Appl. Phys.* **50**, 1026–1030 (1979).
- [16] Hadjipanayis, G. C., Yadlowsky, E. J. & Wollins, S. H. A study of magnetic hardening in $\text{Sm}(\text{Co}_{0.69}\text{Fe}_{0.22}\text{Cu}_{0.07}\text{Zr}_{0.02})_{7.22}$. *J. Appl. Phys.* **53**, 2386 (1982).
- [17] Fidler, J. Coercivity of precipitation hardened cobalt rare earth 17:2 permanent magnets. *J. Magn. Magn. Mater.* **30**, 58 (1982).
- [18] Wong, B. Y., Willard, M. & Laughlin, D. E. Domain wall pinning sites in $\text{Sm}(\text{CoFeCuZr})_x$ magnets. *J. Magn. Magn. Mater.* **169**, 178 (1997).
- [19] Zhang, C. *et al.* The evolution of phase constitution and microstructure in iron-rich 2:17-type Sm-Co magnets with high magnetic performance. *Scientific Reports* **8** (2018).
- [20] Hadjipanayis, G. C., Hazelton, R. C., Lawless, K. R. & Horton, L. S. Magnetic domains in rare-earth cobalt permanent magnets. *IEEE Trans. Magn.* **18**, 1460 (1982).
- [21] Zhang, Y. *et al.* Magnetic hardening studies in sintered $\text{Sm}(\text{Co,Cu}_x\text{,Fe,Zr})_z$ 2:17 high temperature magnets. *J. Appl. Phys.* **87**, 6722 (2000).
- [22] Gutfleisch, O. *et al.* Evolution of magnetic domain structures and coercivity in high-performance SmCo 2:17-type permanent magnets. *Acta Materialia* **54**, 997–1008 (2006).
- [23] Okabe, F. *et al.* Microstructures and magnetic domain structures of sintered $\text{Sm}(\text{Co}_{0.720}\text{Fe}_{0.200}\text{Cu}_{0.055}\text{Zr}_{0.025})_{7.5}$ permanent magnet studied by transmission electron microscopy. *Mat. Trans.* **47**, 218 (2006).
- [24] Sepehri-Amin, H. *et al.* Correlation of microchemistry of cell boundary phase and interface structure to the coercivity of $\text{Sm}(\text{Co}_{0.784}\text{Fe}_{0.100}\text{Cu}_{0.088}\text{Zr}_{0.028})_{7.19}$ sintered magnets. *Acta Materialia* **126**, 1–10 (2017).
- [25] Katter, M., Weber, J., Assmus, W., Schrey, P. & Rodewald, W. A new model for the coercivity mechanism of $\text{Sm}_2(\text{Co,Fe,Cu,Zr})_{17}$ magnets. *IEEE Trans. Magn.* **32**, 4815 (1996).
- [26] Nagel, H. *Hard magnetic materials: rare earth-transition metal and Fe-Nd-B*, vol. 2A1 of *Landolt-Börnstein - Group VIII Advanced Materials and Technologies*, chap. Powder Metallurgy Data (SpringerMaterials, 2003).
- [27] Hellman, F. *et al.* Interface-induced phenomena in magnetism. *Reviews of Modern Physics* **89** (2017).
- [28] Charilaou, M. *et al.* Magnetic properties of ultrathin discontinuous co/pt multilayers: Comparison with short-range ordered and isotropic CoPt_3 films. *Physical Review B* **93** (2016).
- [29] Shen, Y., Leontsev, S., Sheets, A. O., Horwath, J. C. & Turgut, Z. Effect of flake thickness on coercivity of nanocrystalline SmCo_5 bulk prepared from anisotropic nanoflake powder. *AIP Advances* **6**, 056005 (2016).
- [30] Nishida, Y., Endo, M. & Sakurada, S. A modeling study of domain wall pinning in magnets. *Journal of Magnetism and Magnetic Materials* **324**, 1948–1953 (2012).
- [31] Kronmüller, H. & Goll, D. Micromagnetic analysis of pinning-hardened nanostructured, nanocrystalline $\text{Sm}_2\text{Co}_{17}$ based alloys. *Scripta Materialia* **47**, 545–550 (2002).
- [32] Kneller, E. F. & Hawig, R. The exchange-spring magnet: a new material principle for permanent magnets. *IEEE Trans. Magn.* **27**, 3588 (1991).
- [33] Vansteenkiste, A. *et al.* The design and verification of mumax3. *AIP Advances* **4**, 107133 (2014).
- [34] Ahrens, J., Geveci, B. & Law, C. *Visualization Handbook*, chap. ParaView: An End-User Tool for Large Data Visualization (Elsevier, 2005).